



## Nanocrystalline solid solutions $\text{Al}_y\text{Sn}_{1-y}\text{O}_{2-y/2}$ ( $y = 0.57, 0.4$ ) as electrode materials for lithium-ion batteries

Sebastian M. Becker<sup>a,b</sup>, Ibrahim Issac<sup>a</sup>, Ralf Heinzmann<sup>a</sup>, Marco Scheuermann<sup>a,c</sup>, Andreas Eichhöfer<sup>a</sup>, Di Wang<sup>a</sup>, V.S. Kiran Chakravadhanula<sup>a,c</sup>, Christian Kübel<sup>a,c</sup>, Anne S. Ulrich<sup>b,d</sup>, Horst Hahn<sup>a,b,c</sup>, Sylvio Indris<sup>a,b,c,\*</sup>

<sup>a</sup>Institute of Nanotechnology, Karlsruhe Institute of Technology, P.O. Box 3640, 76021 Karlsruhe, Germany

<sup>b</sup>DFG Center for Functional Nanostructures (CFN), Karlsruhe Institute of Technology, Wolfgang-Gaede-Str. 1A, 76131 Karlsruhe, Germany

<sup>c</sup>Helmholtz Institute Ulm (HIU) for Electrochemical Energy Storage, Albert-Einstein-Allee 11, 89069 Ulm, Germany

<sup>d</sup>Institute of Organic Chemistry, Karlsruhe Institute of Technology, Fritz-Haber-Weg 6, 76131 Karlsruhe, Germany

### HIGHLIGHTS

- ▶ Nanocrystalline solid solutions with narrow crystallite size distribution around 5 nm
- ▶ Good cycling stability in Li batteries with specific capacities of 400 mAh g<sup>−1</sup> for 100 cycles.
- ▶ Enhanced performance in comparison to pure SnO<sub>2</sub>.
- ▶ Formation of Li–Al–O matrix that accommodates volume changes during Li–Sn alloy formation.

### ARTICLE INFO

#### Article history:

Received 30 April 2012

Received in revised form

26 November 2012

Accepted 29 November 2012

Available online 12 December 2012

#### Keywords:

Li-ion batteries

Anode material

Aluminum tin oxide

Solid solution

NMR spectroscopy

Mössbauer spectroscopy

### ABSTRACT

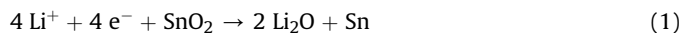
Nanocrystalline  $\text{Al}_y\text{Sn}_{1-y}\text{O}_{2-y/2}$  ( $y = 0.57, 0.4$ ) was investigated as electrode material for lithium-ion batteries. Specific discharge capacities of about 400 mAh g<sup>−1</sup> were obtained for 100 cycles in the case of higher Al content. Electrochemical Li insertion/removal was studied by X-ray diffraction and <sup>7</sup>Li/<sup>27</sup>Al/<sup>119</sup>Sn nuclear magnetic resonance as well as Sn Mössbauer spectroscopy for different Li contents. The formation of a ternary Li–Al–O matrix stabilizes the active Sn metal particles and prevents degradation during alloying with Li.

© 2012 Elsevier B.V. All rights reserved.

## 1. Introduction

Future development of mobile electronic devices and especially electric cars requires new types of lithium-ion batteries with improved storage capacity and cycle life. Since the choice of electrode materials is crucial for the performance of the complete system, many new materials are under investigation [1]. One

example is tin dioxide, SnO<sub>2</sub>, where Li insertion takes place according to the reactions [2,3]:



The second part of this mechanism consists of several steps, during which different Li–Sn alloys are formed up to a maximum content of 4.4 Li per Sn atom [4,5]. This alloying/de-alloying of Li and Sn is accompanied by large volume changes [6] which can lead to a loss of electrical contact within the electrode material and to the current collector and thus to a strong capacity fading [7,8].

\* Corresponding author. Institute of Nanotechnology, Karlsruhe Institute of Technology, P.O. Box 3640, 76021 Karlsruhe, Germany. Tel.: +49 721 608 28312; fax: +49 721 608 26368.

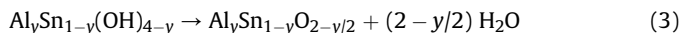
E-mail address: [sylvio.indris@kit.edu](mailto:sylvio.indris@kit.edu) (S. Indris).

Different approaches have been pursued to overcome this problem, including the use of nanostructured samples [9–11] and ternary compounds [12–16]. To our knowledge, there has been only little research on the use of Sn–Al compounds as electrode material in lithium-ion batteries. Samples of Sn–Al alloys have been prepared as thin film by e-beam evaporation [17,18]. Doping of  $\text{SnO}_2$  with 10% Al has also been reported to influence the electrochemical properties [19]. In this work, we have investigated the electrochemical behavior of nanocrystalline solid solutions  $\text{Al}_y\text{Sn}_{1-y}\text{O}_{2-y/2}$  with high Al content ( $y = 0.57, 0.4$ ). The synthesis of the nanocrystalline materials using a coprecipitation method has been described in Ref. [20]. Electrochemical characterization of the compounds includes galvanostatic cycling and cyclic voltammetry. X-ray diffraction (XRD) and transmission electron microscopy (TEM) was used to determine changes in the long-range structure during Li insertion/removal. The changes in the local structure were investigated by  $^7\text{Li}$ ,  $^{27}\text{Al}$ , and  $^{119}\text{Sn}$  nuclear magnetic resonance (NMR) as well as  $^{119}\text{Sn}$  Mössbauer spectroscopy.

## 2. Experimental

Nanocrystalline  $\text{Al}_y\text{Sn}_{1-y}\text{O}_{2-y/2}$  with two different Al contents ( $y = 0.57, 0.4$ ) was prepared by a coprecipitation method using appropriate amounts of  $\text{Al}(\text{NO}_3)_3 \cdot 9\text{H}_2\text{O}$  and  $\text{SnCl}_4 \cdot 5\text{H}_2\text{O}$  [20]. The final step is the calcination of mixed hydroxides  $\text{Al}_y\text{Sn}_{1-y}(\text{OH})_{4-y}$  at different temperatures (450 °C, 550 °C, and 650 °C). This reaction leads to the final products and can be described as:

$$\geq 450\text{ °C}$$



Electrode preparation and cell assembly were carried out in an argon-filled glove box (MBraun, Germany). The electrode films were prepared by mixing the active material ( $\text{Al}_y\text{Sn}_{1-y}\text{O}_{2-y/2}$ ,  $y = 0.57, 0.4$ ), carbon black (Super P, Timcal), and polyvinylidene difluoride (PVDF, Arkema Inc.) in a weight ratio of 80:10:10 in *N*-methyl pyrrolidone (NMP, Sigma Aldrich). The slurry was coated onto a copper foil (Goodfellow, 99.9%) using a doctor blade with a height of 90  $\mu\text{m}$ . The coated film was dried for 48 h. Discs with a diameter of 14 mm were used as working electrodes in coin-type cells (CR2032). Celgard microporous trilayer membrane (PP/PE/PP) was used as separator. Swagelok cells with a mixture of active material (90% by weight) and carbon black (10% by weight) were utilized when the microstructure of the samples was to be investigated after cycling. All cells contained a counter electrode of Li metal (Goodfellow, 99.9%), and an electrolyte of 1 M  $\text{LiPF}_6$  dissolved in a 1:1 (v/v) mixture of ethylene carbonate (EC) and dimethyl carbonate (DMC) provided by Ferro Fine Chemicals. The electrochemical characterization was carried out on a VMP3 potentiostat/galvanostat (Bio-Logic, France). Cyclic voltammetry (CV) measurements were performed with a scan rate of  $0.05\text{ mV s}^{-1}$  in the voltage range from 0.02 to 2.80 V. XRD patterns were measured on an STOE STADI P diffractometer (Cu-K $\alpha$  radiation, Germanium monochromator, Debye-Scherrer geometry) in sealed glass capillaries.

$^{27}\text{Al}$ ,  $^{119}\text{Sn}$ , and  $^7\text{Li}$  magic-angle spinning (MAS) NMR was performed at room temperature on Bruker Avance spectrometers at different magnetic fields. A field of 4.7 T was used for  $^7\text{Li}$  NMR corresponding to a Larmor frequency of  $\nu_L = 77.8\text{ MHz}$ .  $^{119}\text{Sn}$  NMR on intercalated samples ( $x > 0$ ) was performed at 7.0 T ( $\nu_L = 111.8\text{ MHz}$ ). A field of 14.1 T was applied for  $^{27}\text{Al}$  NMR and  $^{119}\text{Sn}$  NMR on the pristine materials ( $x = 0$ ), corresponding to Larmor frequencies of 156.3 MHz and 223.6 MHz, respectively.  $^{119}\text{Sn}$  NMR at 7.0 T was done with 4 mm rotors at a spinning speed of

10 kHz in dry nitrogen atmosphere. Experiments at 4.7 T and 14.1 T were performed with 2.5 mm rotors at a spinning speed of 25 kHz in dry nitrogen atmosphere. An aqueous 1 M  $\text{Al}(\text{NO}_3)_3$  solution was used as the reference for the chemical shift of  $^{27}\text{Al}$  (0 ppm).  $^{119}\text{Sn}$ -enriched  $\text{SnO}_2$  powder was used as  $^{119}\text{Sn}$  reference (−603.4 ppm). A 1 M LiCl solution served as  $^7\text{Li}$  reference (0 ppm). The typical values for the recycling delay of  $^{27}\text{Al}$ ,  $^{119}\text{Sn}$ , and  $^7\text{Li}$  were 5 s, 60 s, and 1 s, respectively.  $^{119}\text{Sn}$  and  $^7\text{Li}$  1D MAS NMR experiments were performed with a rotor synchronized Hahn-echo sequence ( $\pi/2 - \tau - \pi - \tau$ -acquisition) and a typical  $\pi/2$  pulse length of 2  $\mu\text{s}$ .  $^{27}\text{Al}$  1D MAS NMR experiments were recorded with a one pulse experiment ( $\pi/18$ -acq.). In view of the quadrupolar moment of aluminum the used  $\pi/18$  pulse length was less than 0.9  $\mu\text{s}$ . Mestre-C 2.3a and DMFit (2010) were used to evaluate all NMR spectra.

TEM analysis was performed using an image corrected FEI Titan 80–300 operated at an acceleration voltage of 300 kV and equipped with a Gatan US1000 slow-scan CCD camera providing an information limit of 0.8 Å in TEM mode. STEM operation was performed with a nominal spot size of  $\sim 0.5\text{ nm}$  for elemental mapping with an EDAX S-UTW EDX detector. For TEM sample preparation, the powders were directly deposited on 200 mesh holey carbon coated copper grids (Quantifoil).

$^{119}\text{Sn}$  Mössbauer spectroscopic measurements were carried out in transmission mode at room temperature.  $^{119}\text{Sn}$ -enriched  $\text{CaSnO}_3$  was used as  $\gamma$ -ray source. The velocity scale was calibrated with  $\text{SnO}$ , powder which has an isomer shift of  $2.63\text{ mm s}^{-1}$  and a quadrupole splitting of  $1.30\text{ mm s}^{-1}$  [21,22].

## 3. Results and discussion

$\text{Al}_y\text{Sn}_{1-y}\text{O}_{2-y/2}$  ( $y = 0.57, 0.4$ ) samples obtained by the coprecipitation method possess a rutile structure in which a solid solution is formed especially for synthesis temperatures  $\geq 550\text{ °C}$  [20]. The crystallite sizes are in the range of 5–10 nm as shown in a representative TEM image of  $\text{Al}_{0.57}\text{Sn}_{0.43}\text{O}_{1.71}$  heated to 550 °C (Fig. 1).

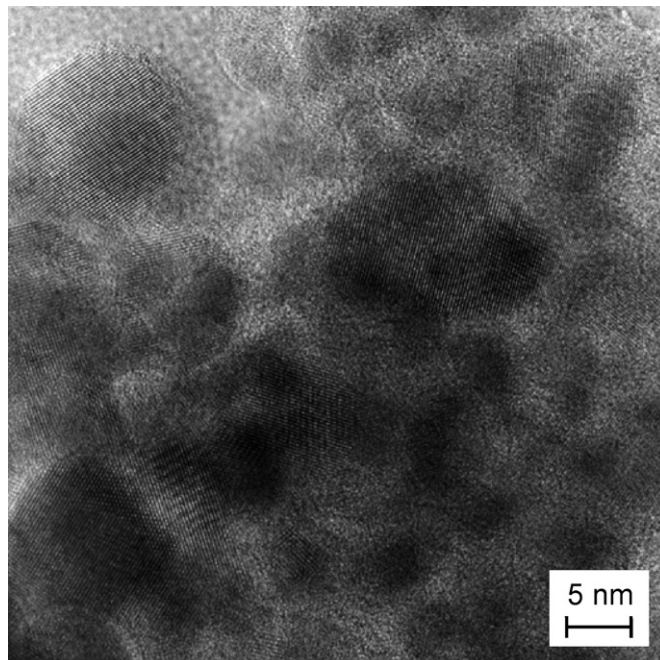


Fig. 1. TEM image of  $\text{Al}_{0.57}\text{Sn}_{0.43}\text{O}_{1.71}$  after heating to 550 °C.

Electrodes consisting of  $\text{Al}_{0.57}\text{Sn}_{0.43}\text{O}_{1.71}$  and  $\text{Al}_{0.4}\text{Sn}_{0.6}\text{O}_{1.8}$ , heated to  $T \geq 450^\circ\text{C}$ , were galvanostatically cycled in the voltage range from 0.02 to 2.8 V with a current density of  $20\text{ mAh g}^{-1}$  (with respect to the total electrode mass). This corresponds to an insertion/removal of 1.8 Li in 20 h per  $\text{Al}_{0.57}\text{Sn}_{0.43}\text{O}_{1.71}$  and 2.1 Li in 20 h per  $\text{Al}_{0.4}\text{Sn}_{0.6}\text{O}_{1.8}$ . Fig. 2 shows the voltage profiles for the first and tenth cycle. The shape of the voltage plateau is similar to those of pure  $\text{SnO}_2$  and  $\text{SnO}$  [2] which suggests that Sn is the active element in these compounds. A clear plateau at about 0.9 V well known for pure  $\text{SnO}_2$  or  $\text{SnO}$  [2] seems to be obscured by the small particle sizes and/or the presence of Al.

During the first discharge, the specific discharge capacities of the  $\text{Al}_{0.4}\text{Sn}_{0.6}\text{O}_{1.8}$  samples are higher than those of the  $\text{Al}_{0.57}\text{Sn}_{0.43}\text{O}_{1.71}$

samples, easily explained by the higher Sn content. In the Li–Al system,  $\text{LiAl}$ ,  $\text{Li}_3\text{Al}_2$  and  $\text{Li}_9\text{Al}_4$  [23] can possibly be formed, but for Al thin film electrodes only  $\text{LiAl}$  has been identified [24]. It is also possible that compounds such as  $\text{Al}_2\text{O}_3$  or  $\text{LiAlO}_2$  are formed during discharge. We calculated the theoretical specific capacities for three different models in order to determine which compounds are formed during the first discharge (Table 1). These capacities include the irreversible component (formation of  $\text{Li}_2\text{O}$  accompanied by the reduction of  $\text{Sn}^{4+}$  to  $\text{Sn}^0$ ) and the contribution of reversible alloying of Li and Sn, equivalent to the reaction steps described in Eqs. (1) and (2) for pure  $\text{SnO}_2$ . In each of the models we assume that there is the reaction of Sn and Li to  $\text{Li}_{4.4}\text{Sn}$ . The first model assumes that the total Al content reacts to  $\text{LiAl}$ , and oxygen forms  $\text{Li}_2\text{O}$ . In the second and third model we assume that Al completely reacts to  $\text{Al}_2\text{O}_3$  and  $\text{LiAlO}_2$ , respectively, and the remaining oxygen forms  $\text{Li}_2\text{O}$ . A comparison with measured capacities shows that the first model results in values that are too high. In contrast, the formation of  $\text{Al}_2\text{O}_3$  or  $\text{LiAlO}_2$ , as assumed in the other two models, seems to be more realistic. The fact that the experimental values are higher by about  $200\text{ mAh g}^{-1}$  can be explained by the formation of the passivating solid–electrolyte interphase (SEI) which gives distinct contributions for these very small particles.

During further cycling,  $\text{Al}_{0.57}\text{Sn}_{0.43}\text{O}_{1.71}$  samples heated to  $550^\circ\text{C}$  and  $650^\circ\text{C}$  show the most stable cycling behavior. This is clearly visible in the voltage profiles of the tenth cycle (Fig. 2).

In Fig. 3 the discharge capacities of the first hundred cycles are shown for all samples. The theoretical capacities for the reversible alloying of Li and Sn amount to  $541\text{ mAh g}^{-1}$  for  $\text{Al}_{0.57}\text{Sn}_{0.43}\text{O}_{1.71}$  and  $639\text{ mAh g}^{-1}$  for  $\text{Al}_{0.4}\text{Sn}_{0.6}\text{O}_{1.8}$ . These values are in good agreement with the experimental values for the second and following cycles (Fig. 3). For the case of high Al content, i.e.  $\text{Al}_{0.57}\text{Sn}_{0.43}\text{O}_{1.71}$ , and temperatures  $\geq 550^\circ\text{C}$ , we achieved high specific capacities with good stability and values of about  $400\text{ mAh g}^{-1}$  for 100 cycles. The original degradation starting at high values in the range of above  $600\text{ mAh g}^{-1}$  is substantially reduced after approx. 20 cycles. Nevertheless, even for these materials the degradation continues even up to 100 cycles. At the elevated temperatures of thermal treatment, it has been reported that a solid solution is formed, with a statistical distribution of Sn and Al on the cation sites and oxygen vacancies on the anion sites [20]. Apparently, this solid solution is beneficial for the cycling behavior. In particular,  $\text{Al}_{0.57}\text{Sn}_{0.43}\text{O}_{1.71}$  heated to  $550^\circ\text{C}$  exhibits good values, also in comparison to literature data for Sn–Al electrode materials. Hu et al. investigated Sn–Al thin film samples with 36 wt% Al which showed  $400\text{ mAh g}^{-1}$  after 60 cycles and strong capacity fading [17]. In case of 60 wt% Al, capacity values of  $500\text{ mAh g}^{-1}$  after 15 cycles have been reported, also with decreasing trend [18].  $\text{SnO}_2$  with doping of 10 at% Al reaches less than  $200\text{ mAh g}^{-1}$  after 34 cycles [19]. Here,  $\text{Al}_{0.4}\text{Sn}_{0.6}\text{O}_{1.8}$  shows decreasing capacities for all sintering temperatures, with best values for the sample heated to  $650^\circ\text{C}$ . However, in order to achieve good cycling performance, it is apparently necessary to have a sufficiently high ratio of Al/Sn.  $\text{Al}_{0.57}\text{Sn}_{0.43}\text{O}_{1.71}$  also has a better performance than pure  $\text{SnO}_2$  synthesized by the same method.  $\text{SnO}_2$

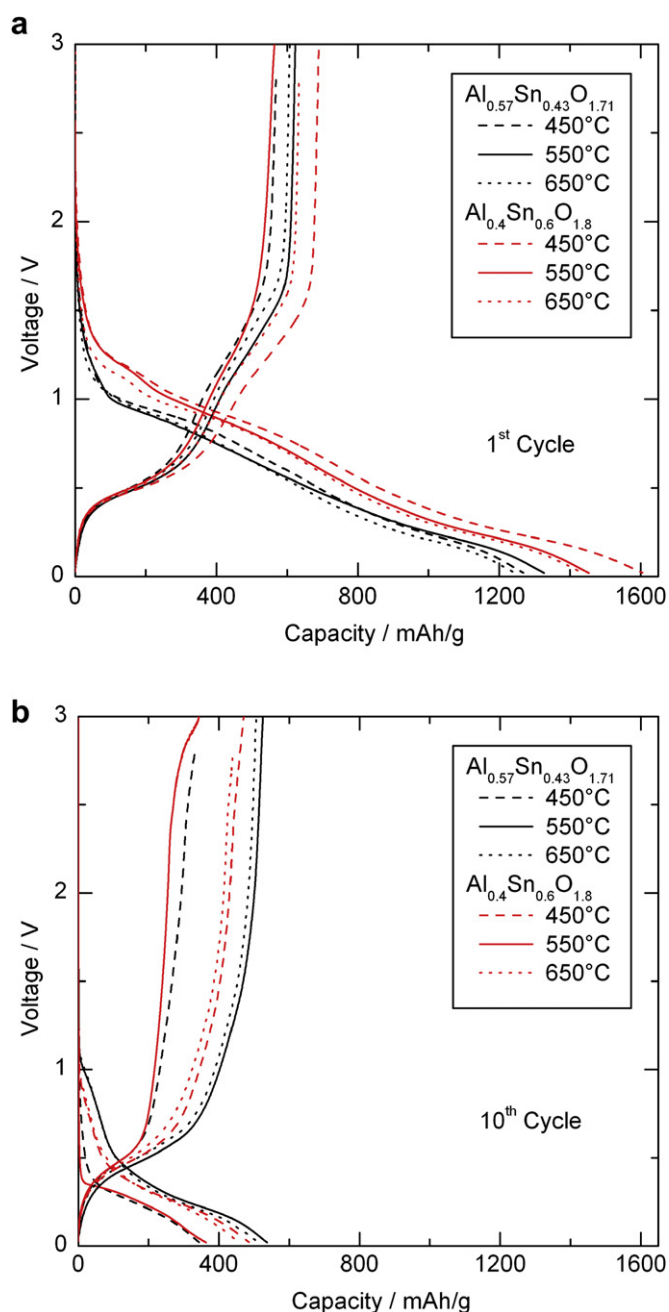
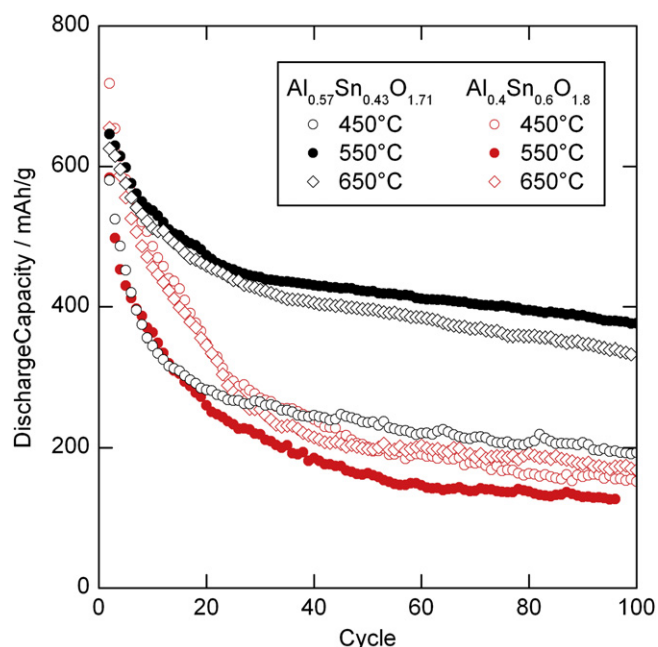


Fig. 2. Voltage profiles during galvanostatic cycling of  $\text{Al}_{0.57}\text{Sn}_{0.43}\text{O}_{1.71}$  and  $\text{Al}_{0.4}\text{Sn}_{0.6}\text{O}_{1.8}$  heated to different temperatures during the first (a) and tenth (b) cycle.

Table 1  
Calculated discharge capacities (irreversible + reversible contributions) in the first cycle under the assumption of formation of different compounds.

Assumed phases formed after first discharge	Theoretical discharge capacity in first cycle [ $\text{mAh g}^{-1}$ ]	
	$\text{Al}_{0.57}\text{Sn}_{0.43}\text{O}_{1.71}$	$\text{Al}_{0.4}\text{Sn}_{0.6}\text{O}_{1.8}$
$\text{Li}_{4.4}\text{Sn} + \text{LiAl} + \text{Li}_2\text{O}$	1684	1950
$\text{Li}_{4.4}\text{Sn} + \text{Al}_2\text{O}_3 + \text{Li}_2\text{O}$	1032	1219
$\text{Li}_{4.4}\text{Sn} + \text{LiAlO}_2 + \text{Li}_2\text{O}$	1032	1219





**Fig. 3.** Discharge capacities of  $\text{Al}_{0.57}\text{Sn}_{0.43}\text{O}_{1.71}$  and  $\text{Al}_{0.4}\text{Sn}_{0.6}\text{O}_{1.8}$  heated to different temperatures during galvanostatic cycling with a current density of  $20 \text{ mAh g}^{-1}$  in the voltage range from 0.02 to 2.8 V. Best values are achieved for samples with high Al content heated to high temperature ( $\geq 550^\circ\text{C}$ ).

shows larger initial capacities but stronger degradation during cycling.

In Fig. 4 the coulombic efficiencies of  $\text{Al}_{0.57}\text{Sn}_{0.43}\text{O}_{1.71}$  samples are shown. After initial irreversible losses, constant values of over 99% are reached, beginning with cycle 20.

The  $\text{Al}_{0.57}\text{Sn}_{0.43}\text{O}_{1.71}$  samples heated to  $550^\circ\text{C}$  and  $650^\circ\text{C}$  initially show quite similar behavior during cycling at a current density of  $20 \text{ mA g}^{-1}$ , before the  $650^\circ\text{C}$  sample slightly declines (Fig. 3). In order to evaluate the performance at higher rates, both samples were cycled with current densities of up to  $800 \text{ mA g}^{-1}$ . Discharge and charge capacities are shown in Fig. 5. The coulombic efficiencies are high for both samples and all current densities. The sample heated to  $550^\circ\text{C}$  reveals a better cycling stability. After applying a series of charging and discharging cycles at high rates and returning to the lower value of  $20 \text{ mA g}^{-1}$ , the capacities revert

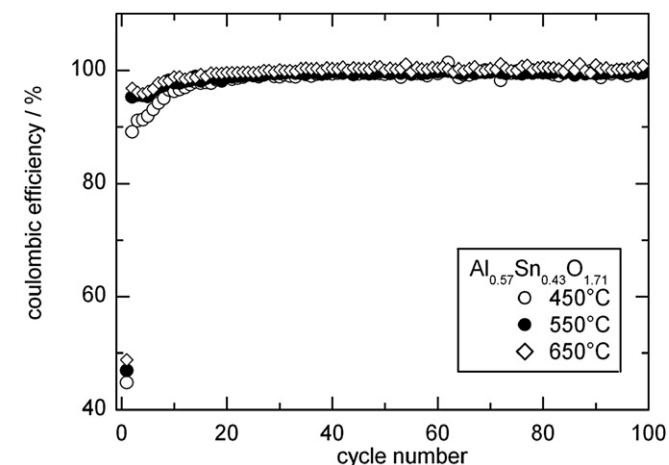


**Fig. 4.** Coulombic efficiency of  $\text{Al}_{0.57}\text{Sn}_{0.43}\text{O}_{1.71}$  samples during galvanostatic cycling with a current density of  $20 \text{ mA g}^{-1}$  in the voltage range of 0.02–2.8 V.

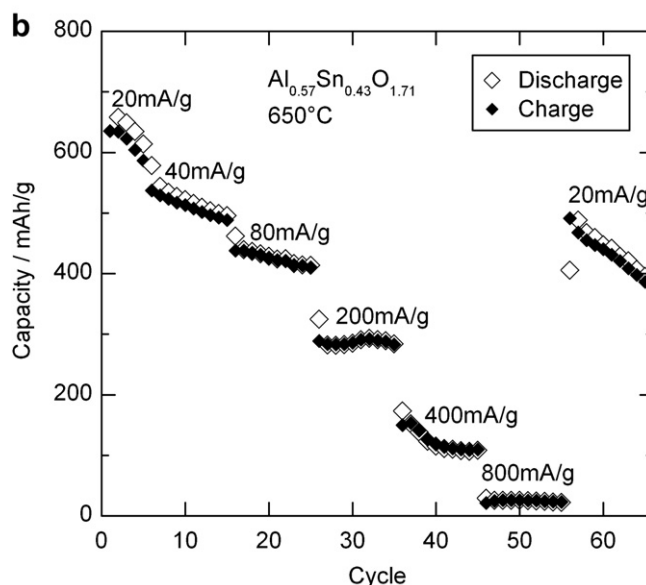
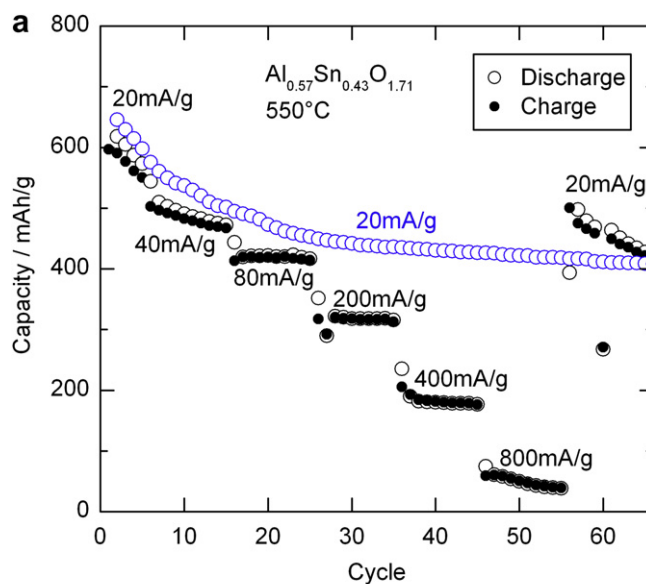


**Fig. 5.** Galvanostatic discharge and charge capacities of  $\text{Al}_{0.57}\text{Sn}_{0.43}\text{O}_{1.71}$  heated to  $550^\circ\text{C}$  (a) and  $650^\circ\text{C}$  (b) during cycling with gradual increase of the current densities to values as high as  $800 \text{ mA g}^{-1}$ .

back to the same level as in the case of constant  $20 \text{ mA g}^{-1}$  cycling. This demonstrates a stable behavior of the material.

Further investigations of the electrochemical behavior of all samples using cyclic voltammetry (CV) are shown in Fig. 6 for the first and tenth cycle. The shape of the CV curves is very similar to those of pure  $\text{SnO}_2$ , Sn metal or Sn alloys [1–5] and the peaks in the range from 1.5 V to 0 V can therefore be ascribed to the formation of the different Li–Sn alloys ( $\text{Li}_2\text{Sn}_5$ ,  $\text{LiSn}$ ,  $\text{Li}_7\text{Sn}_3$ ,...). Since these phases do not occur in a strict subsequent order (see also XRD results described below) these peaks are overlapping in this voltage regime. As in galvanostatic cycling, the enhanced stability of  $\text{Al}_{0.57}\text{Sn}_{0.43}\text{O}_{1.71}$  after heating to  $550^\circ\text{C}$  and  $650^\circ\text{C}$  is obvious. In the CV curves of these samples an additional small reduction peak at about 0.3 V is visible. Reduction peaks found in the lower voltage regime (below 0.5 V) have been reported both for the Li–Sn alloying process [5,25] and, at 0.26 V, for the formation of  $\text{LiAl}$

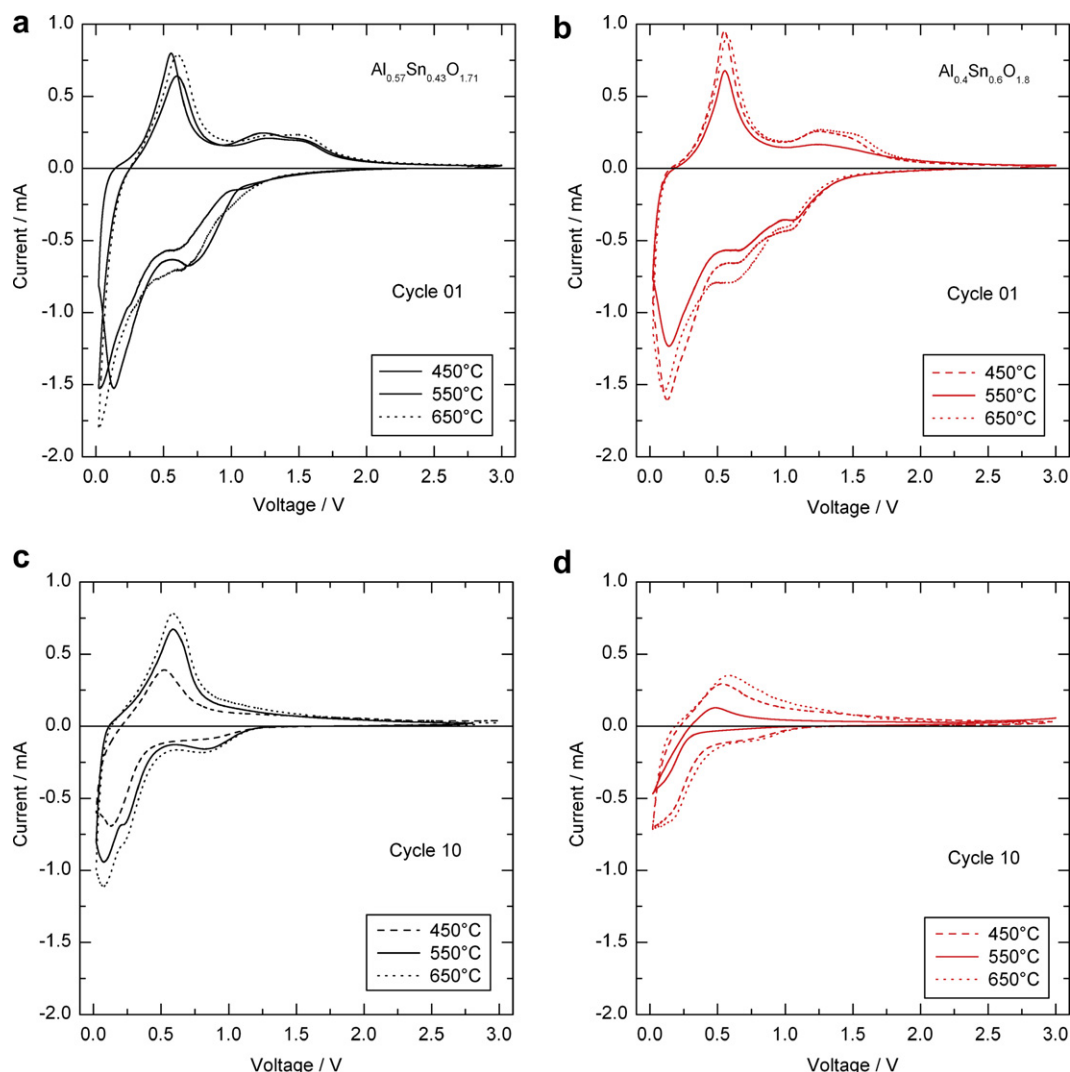


**Fig. 6.** Cyclic voltammograms of the first (top) and tenth (bottom) cycle of  $\text{Al}_{0.57}\text{Sn}_{0.43}\text{O}_{1.71}$  (left) and  $\text{Al}_{0.4}\text{Sn}_{0.6}\text{O}_{1.8}$  samples (right) heated to different temperatures. The scan rate was  $0.05 \text{ mV s}^{-1}$  in each case.

[24]. Thus, the peak at 0.3 V could be a hint that Al is, at least partially, active. Since it could also be correlated to alloying of Li and Sn, further structural investigations are necessary. The corresponding oxidation peaks with a maximum intensity at about 0.6 V can be clearly seen in all CV curves. In Fig. 7 further selected CV cycles of  $\text{Al}_{0.57}\text{Sn}_{0.43}\text{O}_{1.71}$  heated to  $550^\circ\text{C}$  are displayed. It reveals that the intensity of the peak at about 0.3 V is almost constant between the third and tenth cycle. Furthermore, it takes about 10 cycles for the first reduction peak at 1.2 V to disappear. This observation has been taken as a hint for a continuous SEI formation. Due to amorphization of the material new surfaces are created and get in contact with the electrolyte [26]. The formation of  $\text{LiAlO}_2$ , that may take several cycles to be complete, may also contribute to these peaks.

During oxidation, a reaction above 1 V is visible that declines within the first few cycles. Decomposition of  $\text{Li}_2\text{O}$  was reported at oxidation voltages above 1 V [27]. Thus, the observed peak could be a hint that  $\text{Li}_2\text{O}$  is formed during charging in the first cycles.

The electrochemical tests show that  $\text{Al}_{0.57}\text{Sn}_{0.43}\text{O}_{1.71}$  heated to  $550^\circ\text{C}$  reveals the most stable behavior with highest capacity values. For this reason, the investigation of the structural changes that occur during Li insertion/removal in this sample will be

discussed in the following. Fig. 8 shows different states of charge in the first cycle, which were characterized by XRD and MAS NMR. The corresponding XRD patterns are given in Fig. 9. The pattern of the pristine materials reveals very broad peaks and thus small crystallite size of only a few nanometers [20]. The other XRD patterns show that during the first discharge the rutile structure of the pristine material ( $x = 0$ ) is converted irreversibly. The state with  $x = 2.2$  is characterized by broad peaks in the range from  $16^\circ$  to  $50^\circ$ , again representing phases with very small particle sizes. In this range, contributions from the different Li–Sn alloys are expected [28–31]. The fact that only very broad features are visible hinders a clear assignment to crystalline phases. In the patterns of the samples with the highest Li content ( $x = 2.8$  and  $x = 3.8$ ) such broad features are also present at slightly smaller angles. There are only very small contributions from larger particles, e.g. a narrow peak at about  $22.5^\circ$  that is consistent with the strongest peak of  $\text{Li}_{13}\text{Sn}_5$  [30]. These larger crystallites are dissolved during recharging. Crystalline  $\text{LiAlO}_2$  or  $\text{LiAl}$  cannot be identified. The absence of crystalline  $\text{LiAl}$  is in agreement with observations in Al thin film electrodes [24]. During the charge process, the broad peaks shift back to the right, and the patterns for  $x = 2.0$  (charging) and  $x = 2.2$  (discharging) are very similar. For Sn-containing

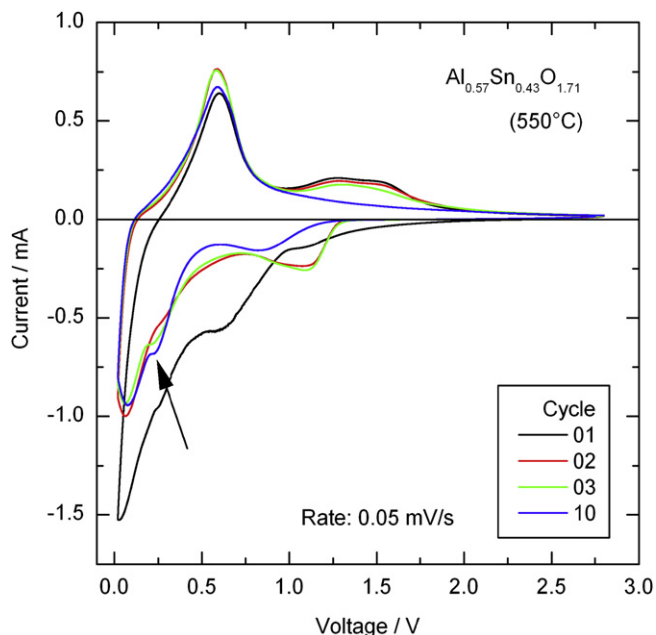


**Fig. 7.** Selected cyclic voltammograms of the first 10 cycles of  $\text{Al}_{0.57}\text{Sn}_{0.43}\text{O}_{1.71}$  heated to 550 °C. The arrow indicates a reduction peak at about 0.3 V, which is almost constant between the third and tenth cycle and may originate from the formation of  $\text{LiAl}$ .

electrodes, aggregation of Sn to larger crystalline particles was reported, which leads to poor cycling performance compared to amorphous or nanostructured material [32–34]. In this sense, the disordered structure of the solid solutions  $\text{Al}_{0.57}\text{Sn}_{0.43}\text{O}_{1.71}$  may be beneficial.

The changes in the local structure of  $\text{Al}_{0.57}\text{Sn}_{0.43}\text{O}_{1.71}$  (550 °C) during insertion and removal of Li were investigated by  $^{27}\text{Al}$ ,  $^{119}\text{Sn}$ ,

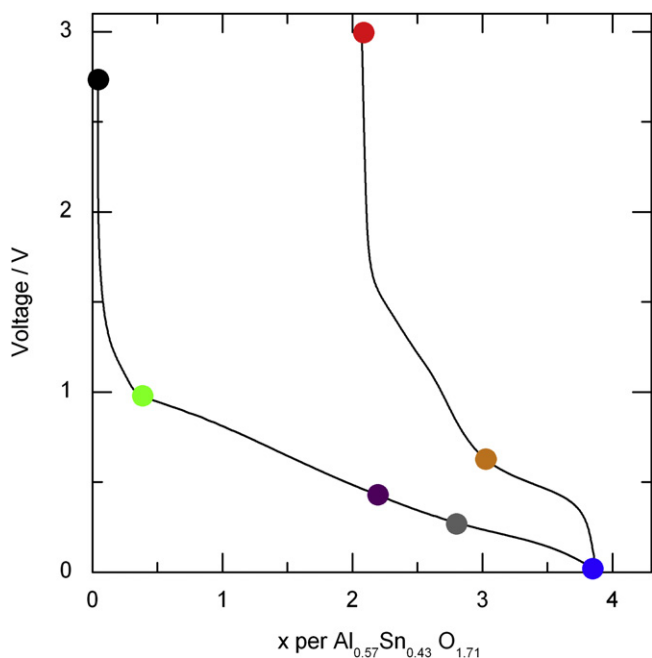


**Fig. 8.** Voltage profile of the first galvanostatic cycle of  $\text{Al}_{0.57}\text{Sn}_{0.43}\text{O}_{1.71}$  heated to 550 °C. Markers indicate samples with different Li contents  $x$  that were characterized by XRD and MAS NMR.

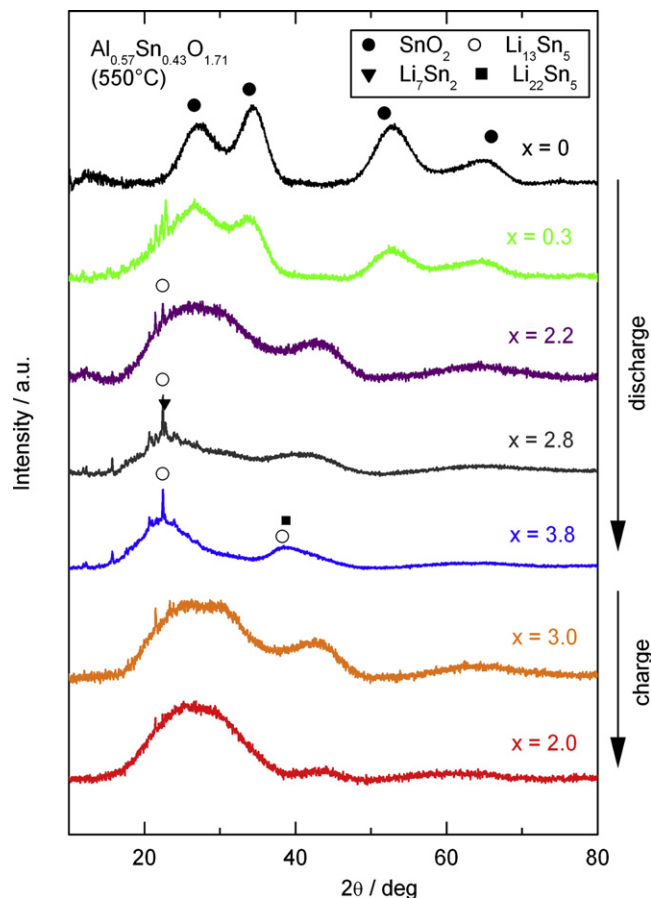


**Fig. 9.** XRD patterns of  $\text{Al}_{0.57}\text{Sn}_{0.43}\text{O}_{1.71}$  heated to 550 °C at different states of charge within the first cycle.

and  $^7\text{Li}$  MAS NMR. The  $^{27}\text{Al}$  NMR spectra displayed in Fig. 10b show strong changes in the range from 0 to 100 ppm during cycling. For the pristine material ( $x = 0$ ) there are three signals at 7 ppm, 36 ppm, and 67 ppm. These can be assigned to Al in an octahedral environment  $[\text{AlO}_6]$ , fivefold coordinated Al  $[\text{AlO}_5]$ , and Al in tetrahedral environment  $[\text{AlO}_4]$  [20].

$^{27}\text{Al}$  NMR spectra of lithiated samples provide further information about the changes in the different local Al environments. During insertion of Li into the structure of  $\text{Al}_{0.57}\text{Sn}_{0.43}\text{O}_{1.71}$ , the occupation of the octahedral environment  $[\text{AlO}_6]$  decreases. Beyond  $x = 2.2$ , a small residual signal at 11 ppm remains during further insertion and removal of Li. It also does not change its position, which indicates that the local structure around octahedrally coordinated Al is not affected by further Li insertion/removal. For Li contents between  $x = 0.3$  and 2.2, also the fivefold coordinated site  $[\text{AlO}_5]$  disappears completely. The occupation of the tetrahedral environment  $[\text{AlO}_4]$  increases in the course of discharge. The frequency of this signal is shifted down-field to the left during the insertion of Li and shifts back to the right during the removal of Li. Anyhow, even in the completely recharged sample, the  $^{27}\text{Al}$  NMR spectrum is clearly different from that of the pristine material ( $x = 0$ ), which shows that the first conversion of the pristine material is irreversible on a local scale.

In order to shed light on the spectral evolution during Li insertion and removal, we also measured  $^{27}\text{Al}$  NMR spectra of  $\alpha$ - and  $\gamma$ - $\text{Al}_2\text{O}_3$ , as well as of  $\text{LiAlO}_2$  (Fig. 11). These phases might be present in  $\text{Al}_{0.57}\text{Sn}_{0.43}\text{O}_{1.71}$  after reaction with Li, as described above. Corundum  $\alpha$ - $\text{Al}_2\text{O}_3$  with its highly symmetric  $[\text{AlO}_6]$  units and

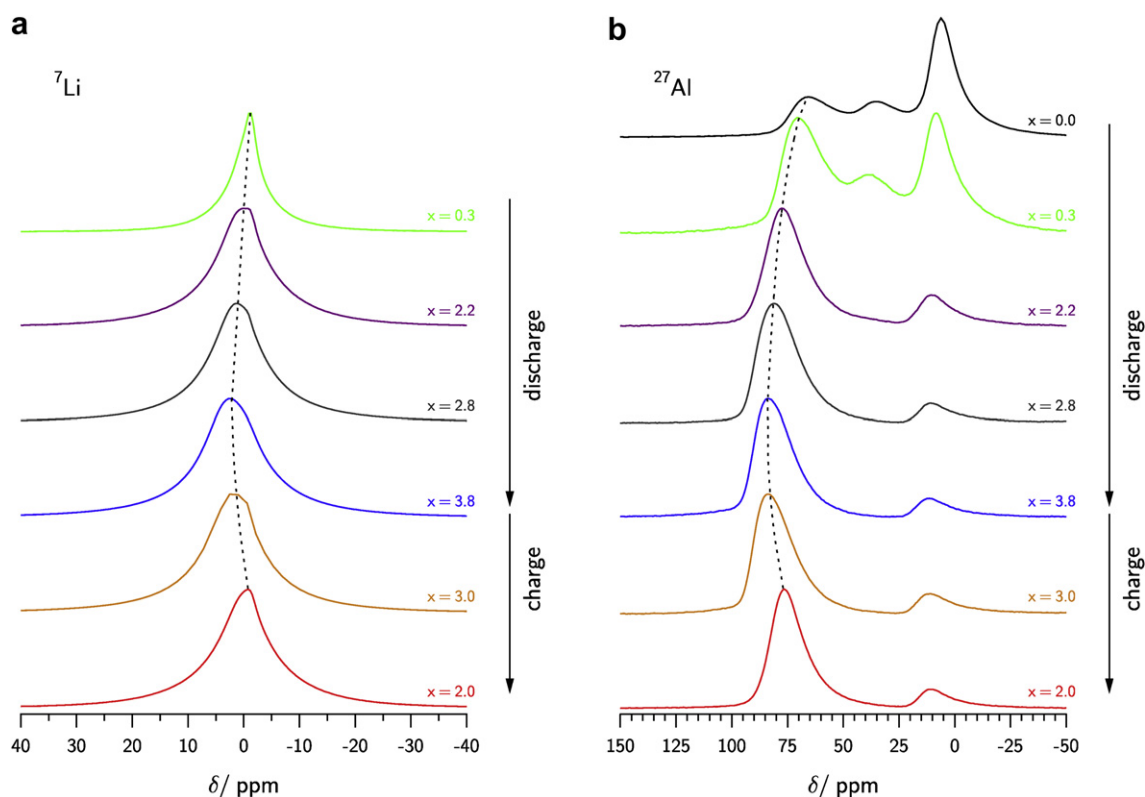


Fig. 10.  $^7\text{Li}$  MAS NMR- (a) and  $^{27}\text{Al}$  MAS NMR spectra (b) of  $\text{Al}_{0.57}\text{Sn}_{0.43}\text{O}_{1.71}$  heated to 550 °C at different states of charge within the first cycle.

a resulting small quadrupole coupling constant shows a narrow peak at 14 ppm. In the case of  $\gamma\text{-Al}_2\text{O}_3$  with its defect spinel structure, Al is in octahedral as well as in tetrahedral crystal sites in a ratio of 2:1. The signals for  $[\text{AlO}_4]$  and  $[\text{AlO}_6]$  are at 11 and 77 ppm, respectively, and are broader because of the more asymmetric environment and correspondingly larger quadrupole coupling constant. Comparison with the spectrum of lithiated  $\text{Al}_{0.57}\text{Sn}_{0.43}\text{O}_{1.71}$ , which is dominated by  $[\text{AlO}_4]$  units, reveals that in lithiated  $\text{Al}_{0.57}\text{Sn}_{0.43}\text{O}_{1.71}$  both  $\text{Al}_2\text{O}_3$  modifications are not present or only to a small extent. The presence of tetrahedral environments  $[\text{AlO}_4]$ , as demonstrated by the spectrum of crystalline  $\text{LiAlO}_2$

(Fig. 11), is well known for ternary Li–Al–O compounds [35,36]. Therefore, our results suggest that in lithiated  $\text{Al}_{0.57}\text{Sn}_{0.43}\text{O}_{1.71}$  the Al is located in a ternary Li–Al–O phase that is structurally disordered, as revealed by XRD (Fig. 9).

The shift of the  $[\text{AlO}_4]$  peak in the  $^{27}\text{Al}$  NMR spectra of  $\text{Al}_{0.57}\text{Sn}_{0.43}\text{O}_{1.71}$  during discharge represents a distortion of the local electronic structure around tetrahedrally coordinated Al. This distortion is caused by the increasing amount of Li that might result in increased mechanical stress due to volume changes of the Li–Sn alloys. After removal of lithium, the distortion of the local structure disappears, which might be a hint that the mechanical stress is released.

Fig. 10a shows  $^7\text{Li}$  MAS NMR spectra of all samples within the first discharge and charge cycle (cf. Fig. 8). All samples show a peak close to 0 ppm. Increasing the lithium content from  $x = 0.3$  to  $x = 2.2$  results in a slight shift of the peak from  $-1.5$  ppm to  $-0.5$  ppm, and the width of the peak doubles from 5.5 ppm to 11.0 ppm (FWHM). Further discharge leads to a shift of the peak to more positive values, while the width shows little change. At the highest lithium content,  $x = 3.8$ , both peak shift and peak width reach their maximum values of 2.4 ppm and 12.2 ppm, respectively. In the spectrum of the recharged sample ( $x = 2.0$ ), the corresponding spectral values are  $-0.8$  ppm for the peak position and 10.6 ppm for the width. Within the experimental errors, the  $^7\text{Li}$  NMR results obtained from the discharged sample with  $x = 2.2$  and from the recharged sample with  $x = 2.0$  are in very good agreement. This observation suggests a reversible change of the lithium environment during discharge and charge between  $x \approx 2.0$  and  $x = 3.8$ . This is consistent with the XRD results described above. The rather strong broadening of the  $^7\text{Li}$  NMR peak at the beginning of the first discharge can be interpreted in terms of an irreversible modification leading to a higher distortion of the local structure. Both findings, the irreversible beginning of the Li insertion and the

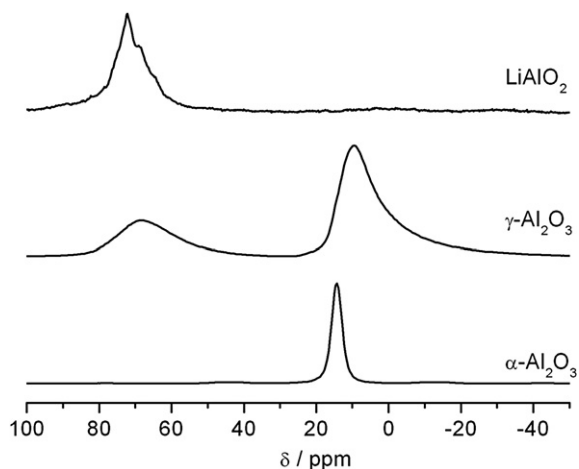


Fig. 11.  $^{27}\text{Al}$  NMR spectra of  $\alpha$ - and  $\gamma\text{-Al}_2\text{O}_3$  and of  $\text{LiAlO}_2$ . In the case of  $\text{LiAlO}_2$ , a dominating contribution of tetrahedral sites  $[\text{AlO}_4]$  is visible in contrast to the  $\text{Al}_2\text{O}_3$  modifications.



subsequent essentially reversible change of local environments can be assigned likewise to the results from  $^{27}\text{Al}$  NMR.

Comparison of the different  $^{119}\text{Sn}$  NMR spectra (Fig. 12) reveals the changes in the Sn environment during Li insertion and removal. The sample without Li ( $x = 0$ ) shows a signal at  $-600$  ppm, which is very close to that of  $\text{SnO}_2$  with  $\text{Sn}^{4+}$  in a rutile structure [37,38]. At the state with  $x = 2.2$ , the signal is shifted to  $-500$  ppm and shows slight broadening. This signal is similar to that of a Li–Sn alloy that can be obtained by reaction of  $\text{SnO}_2$  with 3.5 Li (Fig. 13) [39]. Furthermore, an additional very broad signal appears, which increases in intensity and moves upfield to the right during further reaction to  $x = 3.8$ . This fact provides a strong hint for the conversion of the rutile structure and a considerable distortion of the Sn environment, i.e. the formation of Li–Sn alloys. After recharge and removal of lithium, the very broad signal moves back to the left and has the same chemical shift as for  $x = 2.2$ , but with a much higher intensity than before. Again, this can be explained by a strong increase of local structural disorder. Also for Sn, like in the case of Li and Al, the initial local structural changes during insertion of Li are irreversible, and the initial rutile structure is completely converted. The comparison of  $^{27}\text{Al}$  and  $^{119}\text{Sn}$  NMR also shows that Sn is electrochemically more active than Al. This finding supports the assumption that a stable  $\text{LiAlO}_2$  matrix is formed, in which Sn reacts reversibly with Li.

The activity of Sn was also observed in  $^{119}\text{Sn}$  Mössbauer spectra, which are displayed in Fig. 14. The spectrum of the pristine material shows a doublet with an isomer shift of  $\text{IS} = (0.012 \pm 0.001) \text{ mm s}^{-1}$  and quadrupole splitting  $\text{QS} = (0.682 \pm 0.003) \text{ mm s}^{-1}$ . This corresponds to  $\text{Sn}^{4+}$  cations located at octahedral sites in the rutile structure of  $\text{Al}_{0.57}\text{Sn}_{0.43}\text{O}_{1.71}$  [20]. A small fraction (28%) of this peak is also visible in the spectrum of the fully discharged sample ( $x = 3.8$ ), which may be a hint that during the first discharge a small

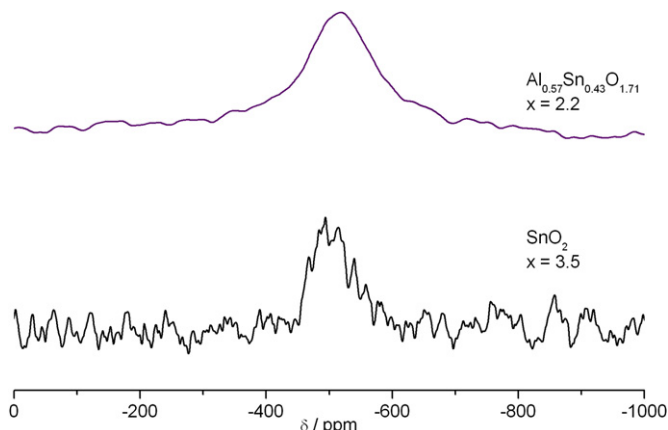


Fig. 13.  $^{119}\text{Sn}$  MAS NMR spectrum of  $\text{Al}_{0.57}\text{Sn}_{0.43}\text{O}_{1.71}$  discharged to  $x = 2.2$ , compared to that of lithiated  $\text{SnO}_2$  with  $x = 3.5$ . In  $\text{SnO}_2$  the full discharge corresponds to  $x = 8.4$ .

fraction of the pristine material did not react with Li. This spectrum is dominated by a doublet with  $\text{IS} = (2.38 \pm 0.04) \text{ mm s}^{-1}$  and  $\text{QS} = (1.05 \pm 0.06) \text{ mm s}^{-1}$ . These values are characteristic of Sn-rich Li–Sn alloys [40]. The degree of absorption is quite low (about 0.4%), which indicates a highly disordered structure. Furthermore, the large quadrupole splittings in both spectra reveal a high degree of asymmetry around the Sn atoms. Thus, these observations are consistent with the XRD and NMR results.

STEM-EDX investigations of fully discharged  $\text{Al}_{0.57}\text{Sn}_{0.43}\text{O}_{1.71}$  are displayed in Fig. 15. These measurements reveal that Sn is localized in particles with sizes between 5 and 25 nm, corresponding to Sn metal and probably also Li–Sn alloy particles. In contrast to that, O and Al are distributed quite homogeneously in this sample, supporting the assumption that a ternary Li–Al–O compound is formed, in agreement with results from  $^{27}\text{Al}$  MAS NMR.

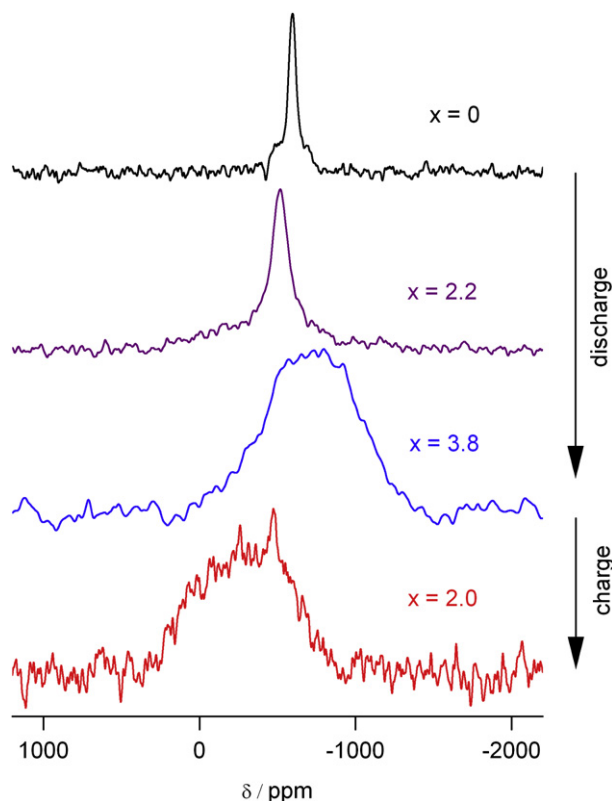


Fig. 12.  $^{119}\text{Sn}$  MAS NMR spectra of  $\text{Al}_{0.57}\text{Sn}_{0.43}\text{O}_{1.71}$  heated to  $550^\circ\text{C}$  at different states of charge.

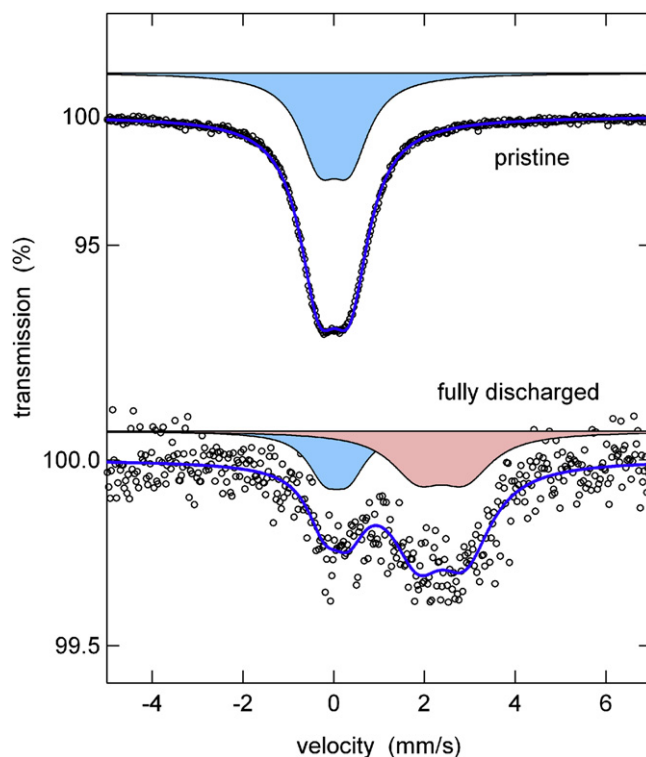
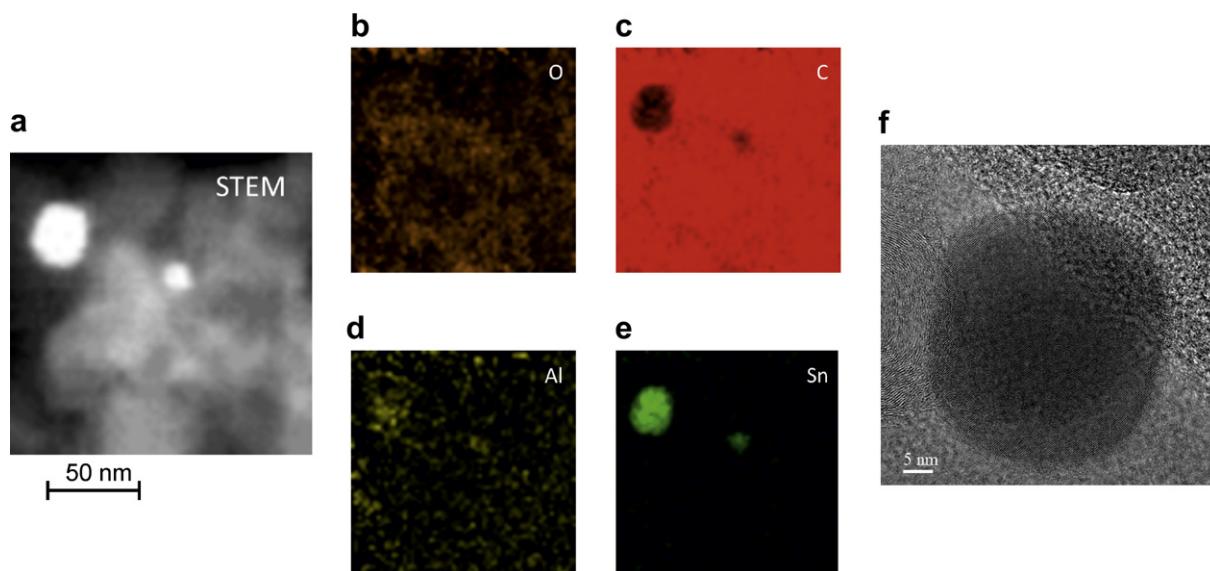


Fig. 14.  $^{119}\text{Sn}$  Mössbauer spectra of  $\text{Al}_{0.57}\text{Sn}_{0.43}\text{O}_{1.71}$  heated to  $550^\circ\text{C}$  before cycling ( $x = 0$ , top) and at fully discharged state ( $x = 3.8$ , bottom).





**Fig. 15.** a) STEM image of  $\text{Al}_{0.57}\text{Sn}_{0.43}\text{O}_{1.71}$  heated to 550 °C, after full discharge. (b–e) EDX mapping for O, C, Al, and Sn. (f) HRTEM image of the larger particle exhibiting lattice spacings of  $d = 0.28$  nm in agreement with Sn (011).

#### 4. Conclusions

$\text{Al}_y\text{Sn}_{1-y}\text{O}_{2-y/2}$  ( $y = 0.57, 0.4$ ) calcinated at temperatures of up to 650 °C were tested as electrode material for lithium-ion batteries.  $\text{Al}_{0.57}\text{Sn}_{0.43}\text{O}_{1.71}$  heated to 550 °C shows the best cycling performance, with capacities of about 400 mAh  $\text{g}^{-1}$  after 100 cycles, good stability, and coulombic efficiencies higher than 99%. The existence of a solid solution in the pristine sample and nanocrystalline particles of about 3–15 nm seem to be beneficial for good cycling behavior. The structural changes occurring in this sample during insertion and removal of Li were investigated in detail. XRD shows the conversion of the rutile structure during the first discharge and a highly disordered state after the first charge. The rutile structure is not rebuilt, which is also supported by  $^{27}\text{Al}$  and  $^{119}\text{Sn}$  NMR. Furthermore,  $^{27}\text{Al}$  NMR and STEM-EDX suggest that during discharge ternary Li–Al–O compounds are formed, which becomes apparent from the observed tetrahedrally coordinated Al. The Li–Sn alloying leads to reversible local distortions that are visible in  $^7\text{Li}$  and  $^{27}\text{Al}$  NMR spectra.  $^{119}\text{Sn}$  NMR reveals a transformation from an ordered structure to a disordered state with broad distributions of local environments. These findings are supported by  $^{119}\text{Sn}$  Mössbauer spectra, which reveal a high degree of asymmetry around the Sn atoms and a high degree of structural disorder.  $^{27}\text{Al}$  and  $^{119}\text{Sn}$  NMR also show that Sn is electrochemically more active than Al. These results, together with the STEM-EDX images, again suggest that a Li–Al–O matrix acts as a stable buffer to accommodate the volume changes during Li–Sn alloying/de-alloying. For commercialization, the irreversible capacity occurring in the first cycle is a serious drawback of these compounds, similar to the case of pure  $\text{SnO}_2$ , resulting in a need for pre-lithiation by, e.g., buthyl-lithium [41,42] or metallic Li. An alternative solution would be the direct synthesis of nanocomposites of Sn metal particles in a  $\text{LiAlO}_2$  matrix.

#### Acknowledgment

We are grateful to the German Federal Ministry of Education and Research and to the DFG Center for Functional Nanostructures (CFN) for financial support.

#### References

- [1] W.-J. Zhang, J. Power Sources 196 (2011) 13–24.
- [2] I.A. Courtney, J.R. Dahn, J. Electrochem. Soc. 144 (1997) 2045.
- [3] M. Winter, J.O. Besenhard, Electrochim. Acta 45 (1999) 31–50.
- [4] O. Crosnier, T. Brousse, X. Devaux, P. Fragnaud, D.M. Schleich, J. Power Sources 94 (2001) 169–174.
- [5] R.A. Huggins, J. Power Sources 81–82 (1999) 13–19.
- [6] L.Y. Beaulieu, K.W. Eberman, R.L. Turner, L.J. Krause, J.R. Dahn, Electrochem. Solid-state Lett. 4 (2001) A137–A140.
- [7] T. Brousse, R. Retoux, U. Herterich, D.M. Schleich, J. Electrochem. Soc. 145 (1998) 1–4.
- [8] R. Retoux, T. Brousse, D.M. Schleich, J. Electrochem. Soc. 146 (1999) 2472.
- [9] C. Kim, M. Noh, M. Choi, J. Cho, B. Park, Chem. Mater. 17 (2005) 3297–3301.
- [10] M.-S. Park, G.-X. Wang, Y.-M. Kang, D. Wexler, S.-X. Dou, H.-K. Liu, Angew. Chem. Int. Ed. 46 (2007) 750–753.
- [11] N. Li, C.R. Martin, B. Scrosati, J. Power Sources 97 (2001) 240–243.
- [12] N. Sharma, K. Shaju, G. Rao, B. Chowdari, J. Power Sources 139 (2005) 250–260.
- [13] E. Rönnebro, J. Yin, A. Kitano, M. Wada, T. Sakai, Solid State Ionics 176 (2005) 2749–2757.
- [14] R. Alcántara, G.F. Ortiz, P. Lavela, J.L. Tirado, Electrochem. Commun. 8 (2006) 731–736.
- [15] G. Wang, X.P. Gao, P.W. Shen, J. Power Sources 192 (2009) 719–723.
- [16] I. Issac, M. Scheuermann, S.M. Becker, E. Gil Bardaji, C. Adelman, D. Wang, C. Kübel, S. Indris, J. Power Sources 196 (2011) 9689–9695.
- [17] R. Hu, M. Zeng, C.Y.V. Li, M. Zhu, J. Power Sources 188 (2009) 268–273.
- [18] R. Hu, Q. Shi, H. Wang, M. Zeng, M. Zhu, J. Phys. Chem. C 113 (2009) 18953–18961.
- [19] R. Alcántara, F.J. Fernández-Madrigal, C. Pérez-Vicente, J.L. Tirado, J.C. Jumas, J. Olivier-Fourcade, Chem. Mater. 12 (2000) 3044–3051.
- [20] I. Issac, R. Heinzmann, S.M. Becker, T. Bräuniger, Z. Zhao-Karger, C. Adelman, V.S.K. Chakravadhanula, C. Kübel, A.S. Ulrich, S. Indris, RSC Adv. 2 (2012) 10700–10707.
- [21] R.H. Herber, Phys. Rev. B 27 (1983) 4013–4017.
- [22] M.S. Moreno, R.C. Mercader, Phys. Rev. B 50 (1994) 9875–9881.
- [23] A.J. McAlister, Bull. Alloy Phase Diagr. 3 (1982) 177–183.
- [24] Y. Hamon, T. Brousse, F. Jousse, P. Topart, P. Buvat, D.M. Schleich, J. Power Sources 97–98 (2001) 185–187.
- [25] I.A. Courtney, J. Tse, O. Mao, J. Hafner, J.R. Dahn, Phys. Rev. B 58 (1998) 15583–15588.
- [26] K.-F. Chiu, H.C. Lin, K.M. Lin, T.Y. Lin, D.T. Shieh, J. Electrochem. Soc. 153 (2006) A1038.
- [27] I.A. Courtney, J.R. Dahn, J. Electrochem. Soc. 144 (1997) 2943–2948.
- [28] J.R. Dahn, I.A. Courtney, O. Mao, Solid State Ionics 111 (1998) 289–294.
- [29] U. Frank, W. Müller, H. Schäfer, Z. Naturforsch. B: Anorg. Chem. Org. Chem. 30 (1975) 6–9.
- [30] U. Frank, W. Müller, Z. Naturforsch. B: Anorg. Chem. Org. Chem. 30 (1975) 316–322.
- [31] U. Frank, W. Müller, H. Schäfer, Z. Naturforsch. B: Anorg. Chem. Org. Chem. 30 (1975) 1–5.

- [32] L.Y. Beaulieu, T.D. Hatchard, A. Bonakdarpour, M.D. Fleischauer, J.R. Dahn, *J. Electrochem. Soc.* 150 (2003) A1457.
- [33] J.-H. Kim, G.-J. Jeong, Y.-W. Kim, H.-J. Sohn, C.W. Park, C.K. Lee, *J. Electrochem. Soc.* 150 (2003) A1544.
- [34] Q. Fan, P.J. Chupas, M.S. Whittingham, *Electrochem. Solid-State Lett.* 10 (2007) A274–A278.
- [35] S. Indris, P. Heitjans, R. Uecker, T. Bredow, *Phys. Rev. B* 74 (2006) 245120.
- [36] M. Marezio, *Acta Crystallogr.* 19 (1965) 396.
- [37] C. Cossement, J. Darville, J.-M. Gilles, J.B. Nagy, C. Fernandez, J.-P. Amoureux, *Magn. Reson. Chem.* 30 (1992) 263.
- [38] N.J. Clayden, C.M. Dobson, A. Fern, *J. Chem. Soc. Dalton Trans.* (1989) 843–847.
- [39] S.M. Becker, M. Scheuermann, V. Šepelák, A. Eichhöfer, D. Chen, R. Mönig, A.S. Ulrich, H. Hahn, S. Indris, *Phys. Chem. Chem. Phys.* 13 (2012) 19624–19631.
- [40] S. Naille, J.-C. Jumas, P.-E. Lippens, J. Olivier-Fourcade, *J. Power Sources* 189 (2009) 814–817.
- [41] M. Wagemaker, E.R.H. van Eck, A.P.M. Kentgens, F.M. Mulder, *J. Phys. Chem. B* 113 (2009) 224–230.
- [42] W. Bensch, J. Ophey, H. Hain, H. Gesswein, D. Chen, R. Mönig, P.A. Gruber, S. Indris, *Phys. Chem. Chem. Phys.* 14 (2012) 7509–7516.